Analytica Chimica Acta 1127 (2020) 190–197

Contents lists available at ScienceDirect

Analytica Chimica Acta

journal homepage: www.elsevier.com/locate/aca

Fe_3O_4 NP@ZIF-8/MoS_2 QD-based electrochemiluminescence with nanosurface energy transfer strategy for point-of-care determination of ATP

Yixin Nie , Yang Liu , Qian Zhang , Feng Zhang , Qiang Ma *, Xingguang Su **

Department of Analytical Chemistry, College of Chemistry, Jilin University, Changchun, 130012, China

HIGHLIGHTS

- Fe_3O_4 NP@ZIF-8 was employed as satisfactory catalyst to amplify MoS_2 QDs ECL signal.
- NSET was the interaction between the point dipole of MoS_2 QDs and collective dipoles on the nanometal surface of Au NPs.
- The high-resolution ECL imaging based on the smartphone enabled the point-of-care determination of ATP.

GRAPHICAL ABSTRACT

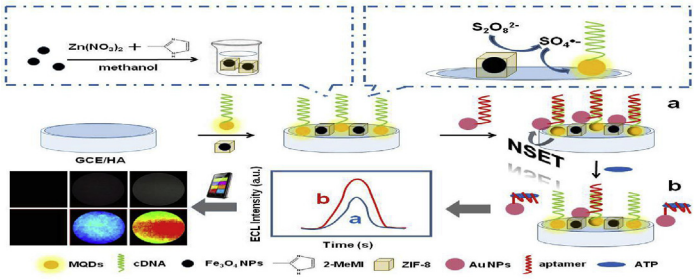

ARTICLE INFO

Article history:
Received 5 March 2020
Received in revised form
16 June 2020
Accepted 20 June 2020
Available online 8 July 2020

Keywords:
MoS_2 quantum dots
Electrochemiluminescence
Fe_3O_4 NP@ZIF-8 complex
Nanosurface energy transfer
ATP detection
ECL digital Imaging

ABSTRACT

Herein, Fe_3O_4 NP@ZIF-8/MoS_2 QD-based electrochemiluminescence (ECL) biosensor with nanosurface energy transfer strategy was successfully developed for point-of-care determination of ATP. With the porous structure and poor electron transfer ability, Fe_3O_4 NP@ZIF-8 complex was first used as an excellent catalyst in ECL. The complex catalyzed the coreactant for more free radicals and hindered the quenching effect of Fe_3O_4 nanoparticles (NPs) on quantum dots (QDs). In ECL-nanosurface energy transfer (NSET) system, through the specific binding of complementary DNA linked to MoS_2 QDs (QDs-cDNA) and aptamer linked to Au NPs, interaction between the point dipole of MoS_2 QDs and the collective dipoles of Au NPs quenched ECL signal. When ATP was captured by aptamer, the ECL-NSET system was taken apart, which resulted in the recovery of ECL signal. Moreover, changes of the ECL imaging can be captured by a smartphone, which enabled point-of-care determination of ATP from 0.05 nmol L^{-1} to 200 nmol L^{-1} with LOD of 0.015 nmol L^{-1}. With superior specificity and stability, the sensing system showed significant potential about the application of catalysts coated with ZIF and NSET in point-of-care ECL determination.

1. Introduction

Adenosine triphosphate (ATP) regulates virtually all biological processes of biochemical reaction and cellular metabolism, such as energy transfer, cellular signaling and respiration catalysis [1–3]. Studies have shown that ATP level is closely related to disorders and dysfunction of biological system, such as hypoglycemia and some

* Corresponding author.
** Corresponding author.
E-mail addresses: qma@jlu.edu.cn (Q. Ma), suxg@jlu.edu.cn (X. Su).

https://doi.org/10.1016/j.aca.2020.06.051
0003-2670/

malignant tumors [4,5]. It is of importance to understand integration of ATP in the brain and explore proliferation and apoptosis of cells [6,7]. Various methods were developed for ATP determination, such as performance liquid chromatography [8,9] and mass spectrometry [10] with need for expensive instruments, lengthy time and cumbersome steps. Therefore, it is an essential issue to develop a biosensor with satisfactory convenience, specificity and stability. The electrogenerated chemiluminescence (ECL) technology which combines characteristics of electrochemistry and spectroscopic chemistry has better accuracy and reproducibility with lower background noise [11–13]. In recent years, it has been widely used in biosensing and clinical testing with convincing results [14–17]. Molybdenum disulfide with a 2D hexagonal lattice under weak van der Waals force has amazing chemical luminescence properties [18]. Among the various morphologies of molybdenum disulfide materials, molybdenum disulfide quantum dots with edge effect and quantum confinement effect have superior physical and chemical properties [19], such as low toxicity, high catalysis and excellent biocompatibility [18], which provides conditions for the actual detection of DNA [20], photodynamic therapy [20], hydrogen evolution catalysis [21], bioimaging [22,23], electrochemical and optical sensors [22–24]. In the ECL sensing system, MoS_2 QDs can generate ECL emission with the assistance of the coreactant potassium persulfate.

In order to improve the low ECL efficiency of MoS_2 QDs, the catalyst for activating ECL coreactant (e.g. potassium persulfate) was explored. Studies have shown that magnetite, pyrite, siderite, ilmenite, etc. can be used for the activation of persulfate [25,26]. Magnetite containing ferrous and ferric oxides can activate persulfate by heterogeneous catalytic reaction, similar to the solution interface reaction [27]. The reaction with superoxide radical ($O_2^{\bullet-}$) promotes the formation of more sulfate radicals [28]. However, Fe_3O_4 NPs can easily quench the luminescence of QDs due to charge transfer between Fe_3O_4 NPs and MoS_2 QDs. So it is necessary to ensure the positive catalytic effect of Fe_3O_4 NPs and avoid the negative charge transfer in the ECL process. In recent years, MOFs have been applied to the establishment of catalysis systems [29–32]. As a kind of MOFs, ZIF-8 can increase the amount and stability of the catalyst due to its large specific surface area and stable structure [33]. The porous structure of Fe_3O_4 NP@ZIF-8 complex has abundant pore channels and more active sites exposed in the reaction solution to become a composite catalyst. Meanwhile, ZIF-8 with poor electron transfer ability can hinder the negative effect of Fe_3O_4 NPs on ECL signal.

Furthermore, in fabrication of biosensing systems, Au NPs are considered to be a common energy acceptor in the non-radiative energy transfer. However, the mechanism of energy transfer is still unclear. Because of their special physical structure and chemical properties, Au NPs can act as an acceptor in both Förster resonance energy transfer (FRET) and nanosurface energy transfer (NSET). Compared with dipole-dipole FRET, NSET is based on the interaction between nanometal surface and molecular dipole [34,35] with higher energy transfer efficiency and longer energy transfer distance (e.g., the distance between the binding sites of living cells) [36]. Strouse et al. [37] confirmed that NSET still existed when the distance between the donor and the acceptor was 22 nm which was more than twice the FRET limit. Since the mechanism involved in the ECL-energy transfer mode has not been discussed in depth, it is particularly essential to calculate the distance between the donor and the acceptor and investigate the exact ECL-energy transfer mechanism [38].

In this work, Fe_3O_4 NP@ZIF-8/MoS_2 QD-based biosensor amplifying ECL signal with NSET strategy was developed for point-of-care determination of ATP (as displayed in Scheme 1). QDs-cDNA and Fe_3O_4 NP@ZIF-8 complex were fixed to the electrode surface by hyaluronic acid (HA). On the electrode, Fe_3O_4 NP@ZIF-8 complex can activate persulfate to boost the ECL signal of MoS_2 QDs. Next, Au NPs attached to the ATP aptamer approached MoS_2 QDs and produced NSET, resulting in the decrease of ECL signal. In the sensing process, ATP took the Au NPs away by specific binding to the aptamer, which resulted in recovery of ECL signal. More importantly, with the changes of ATP concentration, changes of ECL signal can be identified by a smartphone for point-of-care determination.

2. Experimental section

Reagents and apparatus, preparation of Fe_3O_4 NP@ZIF-8 complex and production of Au NP-aptamer were exhibited in the supporting information.

2.1. Synthesis of MoS_2 QDs and QDs-cDNA

0.047 g ammonium molybdate tetrahydrate and 0.254 g reduced glutathione were dissolved in 12 mL of ultrapure water. The solution was heated at 180 °C under the microwave-assisted condition for 50 min and then centrifuged for 10 min (10,000 rpm). Yellow supernatant was then collected as MoS_2 QDs solution. 900 μL of MoS_2 QDs solution was mixed with 80 μL of cDNA solution (100 μmol L^{-1}). After stirring for 3 h, the mixture was dialyzed to near neutral pH and stored in a refrigerator for later use.

2.2. The ECL biosensor fabrication

First, the electrode was polished and cleaned with ultrapure water and ethanol to form a mirror-like surface. 6 μL of sodium hyaluronate solution (1 mmol L^{-1}) was dropped onto the electrode and dried. Viscous sodium hyaluronate solution can generate hydrogen bonds with the conjugate due to its rich hydroxyl group. Next, 3 μL of QDs-cDNA solution prepared above and 3 μL of Fe_3O_4 NP@ZIF-8 saturated solution was mixed and dropped onto the electrode. After drying again, 6 μL of Au NP-aptamer solution was dropped onto the electrode and allowed to react at room temperature for 2 h. Finally, the modified electrode was immersed in 100 μL of solution (pH 7.4) with different concentrations of ATP at 37 °C for 1 h. The ECL signals were acquired in PBS (pH 7.4) with 0.025 mol L^{-1} potassium persulfate. Meanwhile, the actual sample testing was performed in human serum to confirm the feasibility of the sensor for clinical application (described in the supporting information).

2.3. Visual test

The CHI 660B electrochemical workstation and a HUAWEI smartphone were used as the visual test device. The coreactant and reaction environment of the system remained unchanged. For avoiding the interference of background light, a black shading box existed in the whole imaging process. Finally, the ECL visual images were exhibited with the CMOS sensor chip (1920 × 1080 pixels) of the smartphone and the high-resolution recognition of images was realized with the help of a self-developed software. The software was developed by Python. The OpenCV library was used for image processing. The gray value of images was calculated as quantitative value and mapped by the color changed continuously from black to red.

3. Results and discussion

3.1. Characterizations of MoS_2 QDs

From the TEM image (as displayed in Fig. 1A), the excellent

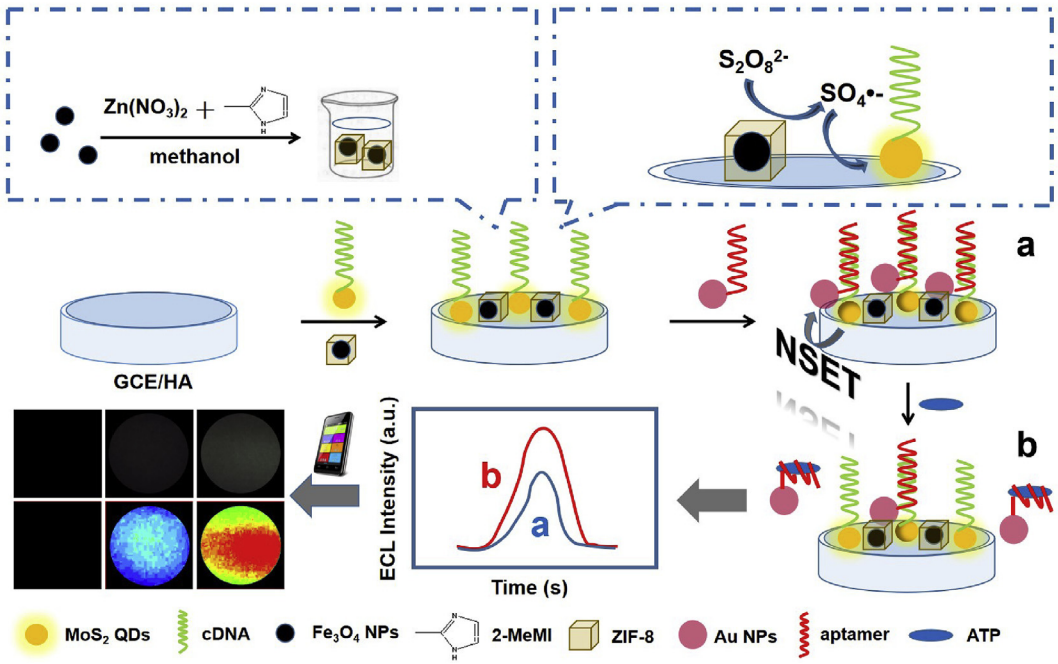

Scheme 1. The Determination Mechanism of the Biosensor.

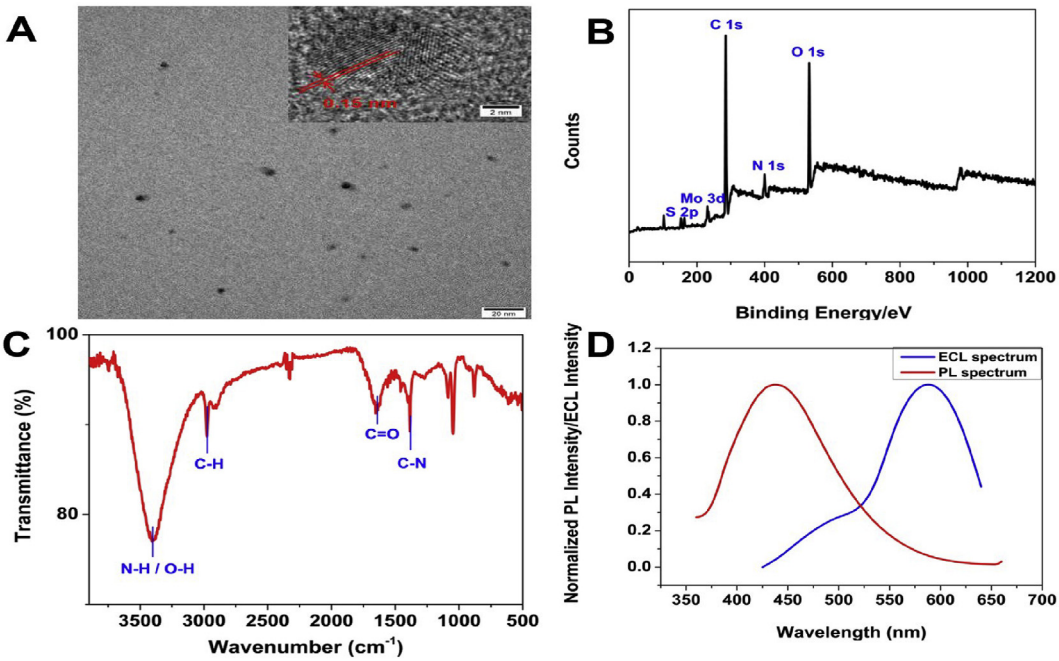

Fig. 1. (A) TEM image, (B) XPS spectrum, (C) FT-IR spectrum, and (D) fluorescence spectrum and ECL spectrum of MoS_2 QDs.

dispersion of MoS_2 QDs with 4 nm of particle size and 0.15 nm of lattice fringes was observed. The conditions about time, temperature and raw material ratio of the synthesis of MoS_2 QDs were optimized. As displayed in Figs. S1A and 50 minutes was the optimal reaction time. The ECL signal increased with the increased reaction temperature (as displayed in Fig. S1B). 180 °C was chosen as the optimal reaction temperature. The best ECL signal of MoS_2 QDs was observed when the molar ratio of ammonium molybdate to glutathione was 1:20 (as displayed in Fig. S1C). The XPS spectrum showed the surface composition of MoS_2 QDs containing C, N, O, Mo and S elements (as displayed in Fig. 1B and Fig. S2). The peak at 227.8 eV represented $Mo^{4+}3d_{5/2}$, which indicated that Mo dominated the 4+ oxidation state. The peak at 163.4 eV represented S $2p_{3/2}$. The peak at 168.7 eV showed the presence of oxidized S^{6+} during the reaction [39,40]. From the UV spectrum (as displayed in Fig. S3), the shoulder peak of MoS_2 QDs was at 310 nm with a significant blue shift compared to conventional MoS_2 nanosheets [41]. From the FT-IR spectrum (as displayed in Fig. 1C), the peak at 3410 cm^{-1} represented stretching vibration of N-H and O-H. The peak at 1700 cm^{-1} represented characteristic stretching vibration

of C=O. And the peak at 1386 cm^{-1} represented stretching vibration of C-N. As displayed in the fluorescence spectrum (Fig. S4), MoS_2 QDs had a property of excitation wavelength dependence from 300 nm to 380 nm. In the ECL spectrum (as displayed in Fig. 1D), the peak position of ECL showed obvious red shift compared with that of fluorescence emission. Since the surface states and defects of MoS_2 QDs played opposite roles in photo and charge injection, red shift of the peak position occurred when the band gap of surface state of MoS_2 QDs was narrower than that of core [42]. The quantum yield of MoS_2 QDs was ca. 4.2% (quinine sulfate 54%).

3.2. Electrochemical feature and characterization of Fe_3O_4 NP@ZIF-8/MoS_2 QDs

HA was applied as the linker of Fe_3O_4 NP@ZIF-8/MoS_2 QDs and electrode surface. At high concentrations, HA solution has significant viscoelasticity due to the three-stage network formed by intermolecular interaction. HA solution at different concentrations of 10^{-6}, 10^{-5}, 10^{-4}, 10^{-3}, and 10^{-2} mol L^{-1} was used for binding of MoS_2 QDs. As displayed in the figure (Fig. S5A), HA solution with decreased viscoelasticity can bind less amount of MoS_2 QDs on the electrode surface, which resulted in low ECL signal. However, with high concentration of HA solution, charge transfer in the ECL reaction can be blocked, and the ECL signal also declined. Therefore, 10^{-3} mol L^{-1} HA solution was the best with the most stability for the following experiments (as shown in Fig. S5B).

As displayed in the TEM image (as shown in Fig. 2A), Fe_3O_4 NP@ZIF-8 complex was with perfect appearance and uniform distribution. The Fe_3O_4 NPs (ca. 15 nm) were successfully coated with ZIF-8 to form core-shell Fe_3O_4 NP@ZIF-8 complex. Fe_3O_4 NP@ZIF-8 complex had a larger pore size and more active sites, which can activate the coreactant [43]. From the XRD patterns (as displayed in Fig. S6), Fe_3O_4 NP@ZIF-8 complex had matching peaks (slight movements) with ZIF-8 and Fe_3O_4 NPs, which represented the successful synthesis of the composite material. In Fig. 2B, the photos of Fe_3O_4 NPs solution and Fe_3O_4 NP@ZIF-8 aqueous solution under magnetic attraction confirmed magnetic properties of Fe_3O_4 NPs and Fe_3O_4 NP@ZIF-8 complex. From Fig. S7, the ECL signal enhanced with the increased amount of Fe_3O_4 NP@ZIF-8 saturated solution. When 3 μL of Fe_3O_4 NP@ZIF-8 saturated solution was added, the ECL signal reached the maximum value. When more Fe_3O_4 NP@ZIF-8 complex was introduced, due to excessive aggregation of Fe_3O_4 NP@ZIF-8 complex can lead to negative interactions of active reaction sites [44], the ECL signal decreased. As displayed in Fig. 2C, the direct contact between Fe_3O_4 NPs and MoS_2 QDs can cause charge transfer, which reduced the ECL signal of MoS_2 QDs by ca. 50%. In the impedance test, the large impedance value (30 kΩ) of ZIF-8 indicated poor conductivity, which hindered the charge transfer between Fe_3O_4 NPs and QDs. This property of ZIF-8 was consistent with previous reports [45,46]. As a result, the ECL signal recovered and increased more than 50%, which confirmed that the complex catalyzed potassium persulfate to form more $SO_4^{\bullet-}$. In the potential-ECL measurements (as displayed in Fig. 2D), the potential of MoS_2 QDs with Fe_3O_4 NP@ZIF-8 complex changed from −2.3 V to −2.1 V compared to the potential of pure MoS_2 QDs, which also proved that Fe_3O_4 NP@ZIF-8 complex catalyzed the formation of $SO_4^{\bullet-}$ from potassium persulfate.

3.3. Mechanism of catalytic ECL and energy transfer

Fe_3O_4 NP@ZIF-8 complex acted as the catalyst to promote potassium persulfate to generate more $SO_4^{\bullet-}$. MoS_2 QDs contacted the $SO_4^{\bullet-}$ generated in the previous step to become excited-state species, resulting in better ECL signal. The mechanism of ECL was presumed as follows:

$$S_2O_8^{2-} + e^- \xrightarrow{Fe_3O_4\ NP@ZIF} SO_4^{\bullet-} + SO_4^{2-} \quad (1)$$

$$SO_4^{\bullet-} + MoS_2\ QDs + e^- \rightarrow MoS_2\ QDs^* + SO_4^{2-} \quad (2)$$

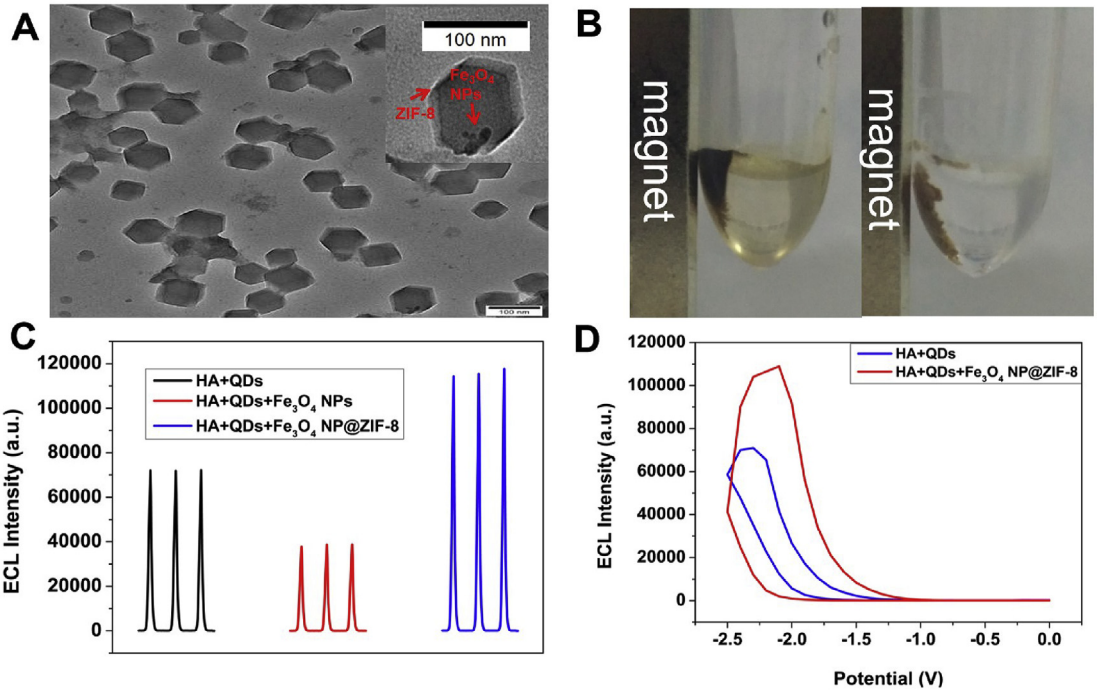

Fig. 2. (A) TEM image of Fe_3O_4 NP@ZIF-8 complex. (B) Photos of Fe_3O_4 aqueous solution and Fe_3O_4 NP@ZIF-8 aqueous solution. (C) ECL curves of MoS_2 QDs with Fe_3O_4 NPs, pure MoS_2 QDs and MoS_2 QDs with Fe_3O_4 NP@ZIF-8 complex and (D) ECL-potential curves of pure MoS_2 QDs and MoS_2 QDs with Fe_3O_4 NP@ZIF-8 complex in PBS (pH = 7.4) containing 0.025 mol L^{-1} potassium persulfate.

$$MoS_2\ QDs^* \rightarrow MoS_2\ QDs + hv \quad (3)$$

Since overlap existed between the ECL spectrum of MoS_2 QDs and the molar absorption spectrum of Au NPs (as displayed in Fig. 3), energy transfer occurred between MoS_2 QDs and Au NPs ($\Phi_{ET} = 0.37$). The mechanism of energy transfer was explored in detail. The different non-radiative energy transfer mechanisms were taken into our consideration, including ECL-FRET and ECL-NSET. The acceptor in ECL-NSET is the nanometal surface equivalent to the assembly of many dipoles rather than a point dipole in ECL-FRET.

In ECL-FRET, according to the previously reported calculation formula [47], the Förster distance R_0 can be calculated when the energy transfer efficiency was 50%, as follows:

$$R_0 = 0.021\left[\kappa 1^2 \Phi_D (n)^{-4} J(\lambda)\right]^{\frac{1}{6}} \quad (4)$$

κ^2 is orientation factor, Φ_D is the quantum yield of MoS_2 QDs, n is water refractive index and $J(\lambda)$ is the overlap integral of ECL spectrum and molar absorption spectrum. The value of R_0 can be calculated as 14.84 nm. It was then substituted into the following formula to calculate the actual distance between MoS_2 QDs and Au NPs (index is 6 for ECL-FRET; 4 for ECL-NSET) [48]:

$$\Phi_{ET} = \frac{1}{1 + \left(\frac{d}{d_0}\right)^n} \quad (5)$$

Since the calculated actual distance was 16.22 nm, it did not match the required distance (less than 10 nm) in ECL-FRET.

In ECL-NSET, according to Persson and Lang' s model [49], when the energy transfer efficiency reached 50%, the distance between MoS_2 QDs and Au NPs can be represented by d_0 as follows:

$$d_0 = \left(\frac{0.225 \Phi_D c^3}{\omega_D^2 \omega_F k_F}\right)^{\frac{1}{4}} \quad (6)$$

Φ_D is the quantum yield of MoS_2 QDs, c is the light velocity, ω_D is the angular frequency of MoS_2 QDs, ω_F is the Au Fermi frequency, and k_F is the Au Fermi wave vector. The value of d_0 was 3.98 nm. And the distance between MoS_2 QDs and Au NPs was 4.55 nm. Therefore, the energy transfer form in the sensing system was ECL-NSET. The energy transfer was the interaction between the point dipole of MoS_2 QDs and the collective dipoles on the nanometal surface of Au NPs.

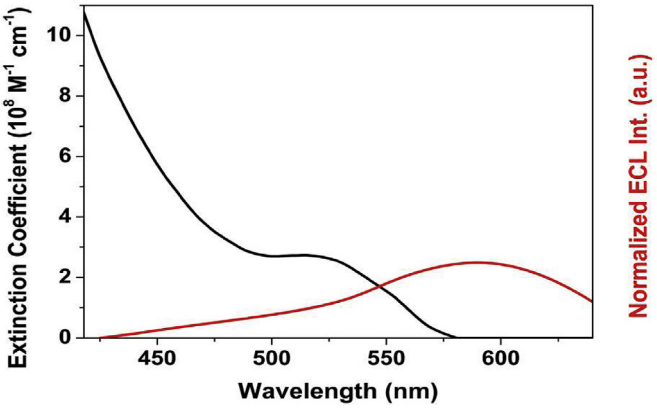

Fig. 3. ECL spectrum of MoS_2 QDs (donor) and molar extinction coefficient curve of Au NPs (acceptor).

3.4. Point-of-care determination of ATP and ECL imaging

From impedance spectra (Fig. S8A), the resistance of the bare electrode was small, and the resistance increased after HA modified. After the modification of Fe_3O_4 NP@ZIF-8/QDs-cDNA to the electrode, resistance increased due to the poor conductivity of ZIF-8. When Au NP-aptamer was introduced, resistance further increased. Both EIS profiles and CV profiles (as displayed in Fig. S8B) verified satisfactory construction of the sensing system. As shown in the qualitative curves (Fig. 4A), without interference from background light, no ECL signal was on the bare electrode. And the ECL signal appeared after the addition of Fe_3O_4 NP@ZIF-8/QDs-cDNA. When Au NP-aptamer was introduced, the ECL quenched due to NSET. When ATP took away the aptamer from the electrode surface, the ECL signal recovered. Meanwhile, in the inter-batch test (Fig. S9), the biosensors produced in five batches had outstanding signal reproducibility, which met the requirements of actual determination. The excellent stability of the biosensor was also displayed in Fig. 4B. The biosensor showed the satisfactory sensitivity for ATP determination from 0.05 nmol L^{-1} to 200 nmol L^{-1} with LOD of 0.015 nmol L^{-1}. The linear equation of logarithm of ATP concentration and the ECL intensity was $I = 10646.8 \log [ATP] + 182052.3$ with a correlation coefficient of 0.992 (as displayed in Fig. 4C and D). The result showed that the biosensing system was convenient to achieve point-of-care determination of ATP. The biosensor showed particularly excellent selectivity for 200 nmol L^{-1} ATP solution compared to 1 μmol L^{-1} other molecules of nucleoside family (CTP, GTP, UTP), histidine, aspartic acid, arginine, glycine, galactose and glucose solution added to the system (as displayed in Fig. S10A). In the anti-interference test, 200 nmol L^{-1} ATP solution was mixed with 1 μmol L^{-1} interfering substances solution mentioned above respectively and introduced into the sensor system. The result confirmed the excellent anti-interference characteristics of the sensor (as displayed in Fig. S10B). Finally, the biosensor was applied for ATP actual determination in human serum using standard addition methods. As displayed in Table S1, the recoveries ranged from 99% to 105% with RSD less than 5.18%. Meanwhile, our method had considerably better sensitivity than other methods for determining ATP (as displayed in Table S2). In particular, our composite sensor had a lower detection limit compared to the sensing system containing MoS_2 QDs or Fe_3O_4 NPs alone. The catalytic effect of Fe_3O_4 NPs on the coreactant effectively amplified the ECL signal of MoS_2 QDs, which made the sensing system more sensitive. To respond to the requirement of actual determination, a visual test based on a smartphone was applied to collect the ECL signals and obtain high-resolution images via self-developed software. As displayed in Fig. 5, the ECL signal cannot be captured by the smartphone when the ATP concentration was 0.05 nmol L^{-1}. When the ATP concentration was 5 nmol L^{-1}, the ECL signal was weak, but the brightness of the image processed by the software was clear. Finally, when the ATP concentration was 200 nmol L^{-1}, the light signal was strong, and the image can be compared with the previous two weaker images after processing. In this ECL imaging for ATP detection, a facile smartphone instead of professional instruments was employed. Furthermore, the detection results were presented by the software in gradual colors. This imaging quantitative method was more intuitive and convenient than the conventional ECL method. Therefore, this detection method based on the smartphone had great potential in ATP point-of-care determination.

4. Conclusions

In the work, a biosensor with high specificity and sensitivity was developed for determining ATP. Fe_3O_4 NP@ZIF-8 complex worked as the catalyst to stimulate the ECL signal of MoS_2 QDs.

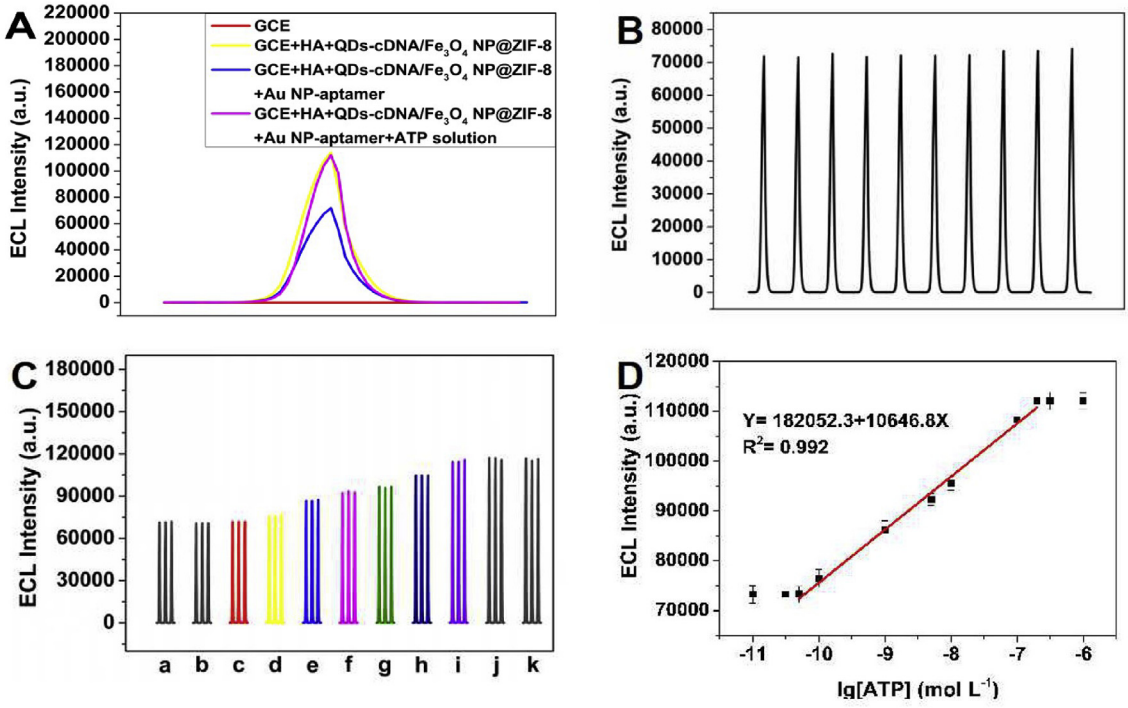

Fig. 4. (A) ECL curves of different modified electrodes, (B) ECL curves of the electrode after modification of sodium hyaluronate, QDs-cDNA, Fe_3O_4 NP@ZIF-8 complex and Au NP-aptamer, (C) ECL curves of proposed biosensor with different concentrations of ATP (from a to k: 10^{-11}, 3×10^{-11}, 5×10^{-11}, 10^{-10}, 10^{-9}, 5×10^{-9}, 10^{-8}, 10^{-7}, 2×10^{-7}, 3×10^{-7}, 10^{-6} mol L^{-1}) in PBS (pH = 7.4) containing 0.025 mol L^{-1} potassium persulfate. (D) Calibration curve for ATP detection.

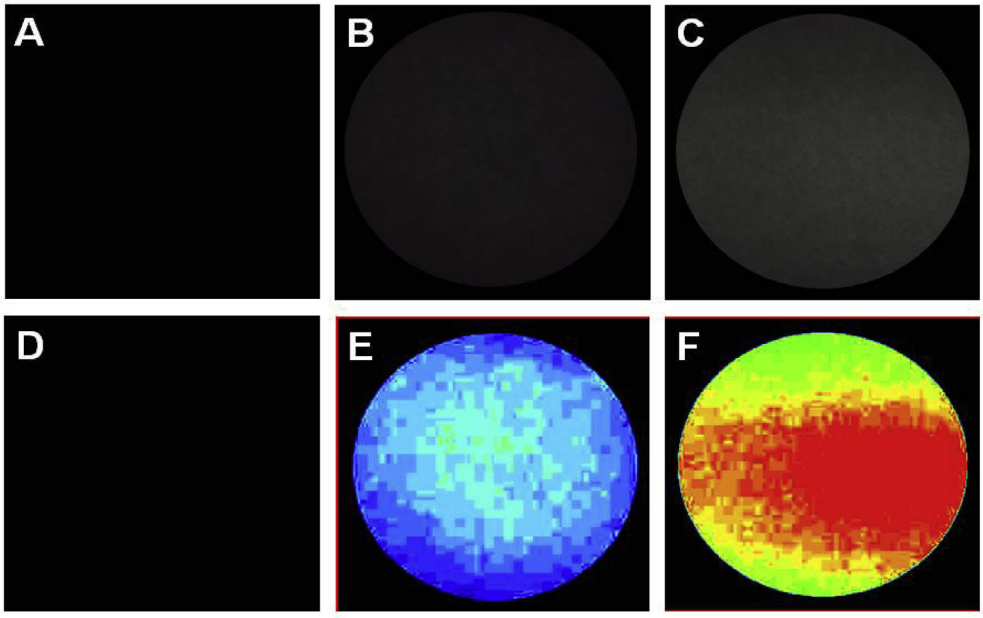

Fig. 5. Digital images (from A to C: 5×10^{-11}, 5×10^{-9}, 2×10^{-7} mol L^{-1} ATP solution) and processed high resolution images (from D to F: 5×10^{-11}, 5×10^{-9}, 2×10^{-7} mol L^{-1} ATP solution) of the ECL emission of the biosensor in PBS (pH = 7.4) containing 0.025 mol L^{-1} potassium persulfate.

Furthermore, the mechanism of ECL energy transfer in the biosensor was deeply explored. The energy transfer was the interaction between the point dipole of MoS_2 QDs and the collective dipoles on the nanometal surface of Au NPs. Most importantly, ECL imaging and high-resolution data processing based on a smartphone and self-developed software enabled the point-of-care determination of ATP. Since point-of-care determination is still an urgent problem to be solved today, we devote to developing a smaller, faster, and more convenient imaging device to achieve the actual tests.

CRediT authorship contribution statement

Yixin Nie: Conceptualization, Data curation, Formal analysis,

Funding acquisition, Investigation, Methodology, Project administration, Resources, Software, Supervision, Validation, Visualization, Writing - original draft, Writing - review & editing. **Yang Liu:** Project administration, Resources. **Qian Zhang:** Software, Supervision. **Feng Zhang:** Visualization. **Qiang Ma:** Writing - original draft. **Xingguang Su:** Writing - original draft.

Declaration of competing interest

The authors declare that they have no known competing financial interests or personal relationships that could have appeared to influence the work reported in this paper.

Acknowledgment

The work was funded by the National Natural Science Foundation of China (No. 21775052, No. 21575048), the Science and Technology Development project of Jilin province, China (No. 20180414013GH), and “Thirteenth Five Year” Project of the Science and Technology Research in the Education Department of Jilin Province, China.

Appendix A. Supplementary data

Supplementary data to this article can be found online at https://doi.org/10.1016/j.aca.2020.06.051.

References

[1] H. Li, Z.J. Guo, W.C. Xie, W.Y. Sun, S. Ji, J. Tian, L. Lv, A label-free fluorometric aptasensor for adenosine triphosphate (ATP) detection based on aggregation-induced emission probe, Anal. Biochem. 578 (2019) 60–65.
[2] J.R. Knowles, Enzyme-catalyzed phosphoryl transfer-reactions, Annu. Rev. Biochem. 49 (1980) 877–919.
[3] C. Dahout-Gonzalez, H. Nury, V. Trézéguet, G. Lauquin, E. Pebay-Peyroula, G. Brandolin, Molecular, functional, and pathological aspects of the mitochondrial ADP/ATP carrier, Physiology 21 (2006) 242–249.
[4] D. Davalos, J. Grutzendler, G. Yang, J.V. Kim, Y. Zuo, S. Jung, D.R. Littman, M.L. Dustin, W.B. Gan, ATP mediates rapid microglial response to local brain injury in vivo, Nat. Neurosci. 8 (2005) 752–758.
[5] Y. Wang, L. Tang, Z. Li, Y. Lin, J. Li, In situ simultaneous monitoring of ATP and GTP using a graphene oxide nanosheet-based sensing platform in living cells, Nat. Protoc. 9 (2014) 1944–1955.
[6] E. Llaudet, S. Hatz, M. Droniou, N. Dale, Microelectrode biosensor for real-time measurement of ATP in biological tissue, Anal. Chem. 77 (2005) 3267–3273.
[7] J. Wang, L. Wang, X. Liu, Z. Liang, S. Song, W. Li, G. Li, C. Fan, A gold nanoparticle-based aptamer target binding readout for ATP assay, Adv. Mater. 19 (2007) 3943–3946.
[8] L. Zhou, X. Xue, J. Zhou, Y. Li, J. Zhao, L. Wu, Fast determination of adenosine 5 '-Triphosphate (ATP) and its catabolites in royal jelly using ultraperformance liquid chromatography, J. Agric. Food Chem. 60 (2012) 8994–8999.
[9] X.F. Xue, F. Wang, J.H. Zhou, F. Chen, Y. Li, J. Zhao, Online cleanup of accelerated solvent extractions for determination of adenosine 5 '-Triphosphate (ATP), adenosine 5 '-Diphosphate (ADP), and adenosine 5 '-Monophosphate (AMP) in royal jelly using high-performance liquid chromatography, J. Agric. Food Chem. 57 (2009) 4500–4505.
[10] D.H. Deng, N. Xia, S.J. Li, C.Y. Xu, T. Sun, H. Pang, L. Liu, Simple, fast and selective detection of adenosine triphosphate at physiological pH using unmodified gold nanoparticles as colorimetric probes and metal ions as cross-linkers, Sensors 12 (2012) 15078–15087.
[11] L. Yang, W.J. Zhu, X. Ren, M.S. Khan, Y. Zhang, B. Du, Q. Wei, Macroporous graphene capped Fe_3O_4 for amplified electrochemiluminescence immunosensing of carcinoembryonic antigen detection based on CeO_2@TiO_2, Biosens. Bioelectron. 91 (2017) 842–848.
[12] L. Yang, Y.Y. Li, Y. Zhang, D.W. Fan, X.H. Pang, Q. Wei, B. Du, 3D nanostructured palladium-functionalized graphene-aerogel-supported Fe_3O_4 for enhanced Ru(bpy)(3)(2+)-Based electrochemiluminescent immunosensing of prostate specific AntigenACS, Appl. Mater. Interfaces. 9 (2017) 35260–35267.
[13] B. Xing, W.J. Zhu, X.P. Zheng, Y.Y. Zhu, Q. Wei, D. Wu, Electrochemiluminescence immunosensor based on quenching effect of SiO_2@PDA on SnO_2/rGO/Au NPs-luminol for insulin detection, Sens. Actuators, B 265 (2018) 403–411.
[14] Y. Zhou, Y. Yu, Y. Chai, R. Yuan, Electrochemical synthesis of silver nanoclusters on electrochemiluminescent resonance energy transfer amplification platform for Apo-A1 detection, Talanta 181 (2018) 32–37.
[15] M.M. Chen, Y. Wang, S.B. Cheng, W. Wen, X. Zhang, S. Wang, W.H. Huang, Construction of highly efficient resonance energy transfer platform inside a nanosphere for ultrasensitive electrochemiluminescence detection, Anal. Chem. 90 (2018) 5075–5081.
[16] X. Chen, W. Gui, Q. Ma, Ultrasensitive detection of EGFR gene based on surface plasmon resonance enhanced electrochemiluminescence of CuZnInS quantum dots, Anal. Chim. Acta 1009 (2018) 73–80.
[17] M.S. Wu, L.J. He, J.J. Xu, H.Y. Chen, RuSi@Ru(bpy)(3)(2+)/Au@Ag_2S nanoparticles electrochemiluminescence resonance energy transfer system for sensitive DNA detection, Anal. Chem. 86 (2014) 4559–4565.
[18] S. Presolski, M. Pumera, Covalent functionalization of MoS_2, mater, Today Off. 19 (2016) 140–145.
[19] Z.X. Gan, L.Z. Liu, H.Y. Wu, Y.L. Hao, Y. Shan, X.L. Wu, P.K. Chu, Quantum confinement effects across two-dimensional planes in MoS_2 quantum dots, Appl. Phys. Lett. 106 (2015), 233113.
[20] H. Dong, S. Tang, Y. Hao, H. Yu, W. Dai, G. Zhao, Y. Cao, H. Lu, X. Zhang, H. Ju, Fluorescent MoS_2 quantum dots: ultrasonic preparation, up-conversion and down-conversion bioimaging, and photodynamic therapy, ACS Appl. Mater. Interfaces 8 (2016) 3107–3114.
[21] X. Ren, L. Pang, Y. Zhang, X. Ren, H. Fan, S. Liu, One-step hydrothermal synthesis of monolayer MoS_2 quantum dots for highly efficient electrocatalytic hydrogen evolution, J. Mater. Chem. A. 3 (2015) 10693–10697.
[22] W. Dai, H. Dong, B. Fugetsu, Y. Cao, H. Lu, X. Ma, X. Zhang, Tunable fabrication of molybdenum disulfide quantum dots for intracellular MicroRNA detection and multiphoton bioimaging, Small 11 (2015) 4158–4164.
[23] C. Sweet, A. Pramanik, S. Jones, P.C. Ray, Two-photon fluorescent molybdenum disulfide dots for targeted prostate cancer imaging in the biological II window, ACS Omega 2 (2017) 1826–1835.
[24] H. Cao, H. Wang, Y. Huang, Y. Sun, S. Shi, M. Tang, Quantification of gold(III) in solution and with a test stripe via the quenching of the fluorescence of molybdenum disulfide quantum dots, Microchim. Acta. 184 (2017) 91–100.
[25] N. Yan, F. Liu, W.Y. Huang, Interaction of oxidants in siderite catalyzed hydrogen peroxide and persulfate system using trichloroethylene as a target contaminant, Chem. Eng. J. 219 (2013) 149–154.
[26] A.L. Teel, M. Ahmad, R.J. Watts, Persulfate activation by naturally occurring trace minerals, J. Hazard Mater. 196 (2011) 153–159.
[27] M. Usman, P. Faure, C. Ruby, Application of magnetite-activated persulfate oxidation for the degradation of PAHs in contaminated soils, Chemosphere 87 (2012) 234–240.
[28] G.D. Fang, D.D. Dionysiou, S.R. Al-Abed, Superoxide radical driving the activation of persulfate by magnetite nanoparticles: implications for the degradation of PCBs, Appl. Catal. B Environ. 129 (2013) 325–332.
[29] X.M. Lin, F.Q. Luo, L.Y. Zheng, G.M. Gao, Y.W. Chi, Fast, sensitive, and selective ion-triggered disassembly and release based on tris(bipyridine)ruthenium(II)-Functionalized metal-organic frameworks, Anal. Chem. 87 (2015) 4864–4870.
[30] X.M. Lin, G.M. Gao, L.Y. Zheng, Y.W. Chi, G.N. Chen, Encapsulation of strongly fluorescent carbon quantum dots in metal-organic frameworks for enhancing chemical sensing, Anal. Chem. 86 (2014) 1223–1228.
[31] H.M. Ma, X.J. Li, T. Yan, Y. Li, Y. Zhang, D. Wu, Q. Wei, B. Du, Electrochemiluminescent immunosensing of prostate-specific antigen based on silver nanoparticles-doped Pb (II) metal-organic framework, Biosens. Bioelectron. 79 (2016) 379–385.
[32] Y. Xu, X.B. Yin, X.W. He, Y.K. Zhang, Electrochemistry and electrochemiluminescence from a redox-active metal-organic framework, Biosens. Bioelectron. 68 (2015) 197–203.
[33] C.Y. Xiong, W.B. Liang, Y.N. Zheng, Y. Zhuo, Y.Q. Chai, R. Yuan, Ultrasensitive assay for telomerase activity via self-enhanced electrochemiluminescent ruthenium complex doped metal-organic frameworks with high emission efficiency, Anal. Chem. 89 (2017) 3222–3227.
[34] P.K. Sarkar, N. Polley, S. Chakrabarti, P. Lemmens, S.K. Pal, Nanosurface energy transfer based highly selective and ultrasensitive "turn on" fluorescence mercury sensor, ACS Sens. 1 (2016) 789–797.
[35] C. Chen, C. Midelet, S. Bhuckory, N. Hildebrandt, M.H.V. Werts, Nanosurface energy transfer from long-lifetime terbium donors to gold nanoparticles, J. Phys. Chem. C 122 (2018) 17566–17574.
[36] X. Wu, H. Liu, D. Han, B. Peng, H. Zhang, L. Zhang, J. Li, J. Liu, C. Cui, S. Fang, M. Li, M. Ye, W. Tan, Elucidation and structural modeling of CD71 as a molecular target for cell-specific aptamer binding, J. Am. Chem. Soc. 141 (2019) 10760–10769.
[37] C.S. Yun, A. Javier, T. Jennings, M. Fisher, S. Hira, S. Peterson, B. Hopkins, N.O. Reich, G.F. Strouse, Nanometal surface energy transfer in optical rulers, breaking the FRET barrier, J. Am. Chem. Soc. 127 (2005) 3115–3119.
[38] L. Yang, D.W. Fan, Y. Zhang, C.F. Ding, D. Wu, Q. Wei, H.X. Ju, Ferritin-based electrochemiluminescence nanosurface energy transfer system for procalcitonin detection using HWRGWVC heptapeptide for site-oriented antibody immobilization, Anal. Chem. 91 (2019) 7145–7152.
[39] W. Gu, Y.H. Yan, C.L. Zhang, C.P. Ding, Y.Z. Xian, One-step synthesis of water-soluble MoS_2 quantum dots via a hydrothermal method as a fluorescent probe for hyaluronidase detection, ACS Appl. Mater. Interfaces 8 (2016) 11272–11279.
[40] Y. Wang, Y.N. Ni, Molybdenum disulfide quantum dots as a photoluminescence sensing platform for 2,4,6-trinitrophenol detection, Anal. Chem. 86 (2014) 7463–7470.
[41] X. Ren, L. Pang, Y. Zhang, X. Ren, H. Fan, S. Liu, One-step hydrothermal synthesis of monolayer MoS_2 quantum dots for highly efficient electrocatalytic hydrogen evolution, J. Mater. Chem. A. 3 (2015) 10693–10697.

[42] L.F. Sun, L. Bao, B.R. Hyun, A.C. Bartnik, Y.W. Zhong, J.C. Reed, D.W. Pang, H.D. Abruña, G.G. Malliaras, F.W. Wise, Electrogenerated chemiluminescence from PbS quantum dots, Nano Lett. 9 (2009) 789–793.
[43] S. Sajjadi, A. Khataee, R.D.C. Soltani, N. Bagheri, A. Karimi, A.E.F. Azar, Implementation of magnetic Fe_3O_4@ZIF-8 nanocomposite to activate sodium percarbonate for highly effective degradation of organic compound in aqueous solution, J. Ind. Eng. Chem. 68 (2018) 406–415.
[44] R.D.C. Soltani, S. Jorfi, M. Safari, M.-S. Rajaei, The impact social marketing mix dimensions on the prevention of drug abuse case study (male secondary school students of Isfahan province), J. Environ. Manag. 179 (2016) 47.
[45] C. Xiong, W. Liang, Y. Zheng, Y. Zhuo, Y. Chai, R. Yuan, Ultrasensitive assay for telomerase activity via self-enhanced electrochemiluminescent ruthenium complex doped metal-organic frameworks with high emission efficiency, Anal. Chem. 89 (2017) 3222–3227.
[46] R. Zang, Y. He, R. Yuan, Y. Chai, An ultrasensitive electrochemiluminescence immunosensor based on zeolitic imidazolate frameworks encapsulating spherical graphite crystals, J. Electroanal. Chem. 781 (2016) 284–288.
[47] C. Chen, C. Midelet, S. Bhuckory, N. Hildebrandt, M.V. Werts, Nanosurface energy transfer from long-lifetime terbium donors to gold nanoparticles, J. Phys. Chem. C 122 (2018) 17566–17574.
[48] R. Prajapati, S. Chatterjee, A. Bhattacharya, T.K. Mukherjee, Surfactant-Induced modulation of nanometal surface energy transfer from silicon quantum dots to silver nanoparticles, J. Phys. Chem. C 119 (2015) 13325–13334.
[49] T.L. Jennings, M.P. Singh, G.F. Strouse, Fluorescent lifetime quenching near d=1.5 nm gold nanoparticles: probing NSET validity, J. Am. Chem. Soc. 128 (2006) 5462–5467.